Domain-engineered, aperiodically-poled KTiOPO$_4$ for polarization-entangled photons

PAULINA S. KUO,[1,*] CH. S. S. PAVAN KUMAR,[1] ANOUAR RAHMOUNI,[1] DILEEP V. REDDY,[2,3] ORI LEVIN,[4] AND NOA VOLOCH BLOCH[4]

[1] *Information Technology Laboratory, National Institute of Standards and Technology, 100 Bureau Drive, Gaithersburg, MD 20899, USA*
[2] *Physical Measurement Laboratory, National Institute of Standards and Technology, 325 Broadway, Boulder, CO 80305, USA*
[3] *Department of Physics, University of Colorado, Boulder, CO 80309, USA*
[4] *Raicol Crystals, 22 Hamelacha Street, Rosh Ha'Ayin, 4809162 Israel*
[*] *paulina.kuo@nist.gov*

Abstract: We demonstrate a high-quality source of polarization-entangled photons in aperiodically-poled KTiOPO$_4$ (KTP). The crystal is based on a phase-modulated domain-engineered design that allows two simultaneous downconversion processes, where the two processes correspond to the two terms of the entangled-photon state. We characterized the temperature tuning of both the spectral response and the polarization-fringe visibility for spontaneous parametric downconversion (SPDC) using this crystal. At the optimum temperature where wavelength distinguishability of the two SPDC processes is smallest, we obtained average polarization-entanglement visibility 0.984 ± 0.003 with a measured Clauser–Horne–Shimony–Holt (CHSH) parameter $S = 2.801 \pm 0.014$. We also discuss effects of the relative phase in the entangled-photon state and present a new way to compensate for these effects to obtain high polarization-entanglement visibility.

1. Introduction

Entangled photon pairs are a key resource for quantum networking [1], quantum communications [2, 3], quantum-enhanced sensing [4] and photonic quantum computing [5]. For photonic quantum computing, the generation of entangled photonic states plays a crucial role as these states enable the realization of entanglement, quantum interference, and scalable quantum logic operations. The entangled photons are typically produced by spontaneous parametric downconversion (SPDC) [6–12] (or spontaneous four-wave mixing (SFWM) [13, 14]) where a higher energy pump photon (or a pair of pump photons for SFWM) spontaneously decays into a pair of lower energy photons, called the signal and idler. The signal and idler photons are correlated in many degrees of freedom including time, frequency and polarization. A typical entangled quantum state can be written as

$$|\Psi\rangle \quad = \quad \sqrt{\epsilon}|10\rangle + e^{i\phi}\sqrt{1-\epsilon}|01\rangle, \tag{1}$$

where $|0\rangle$ and $|1\rangle$ represent orthogonal states, ϵ is the amplitude mismatch factor and ϕ is the relative phase. The factor ϵ should ideally equal 0.5 so that the amplitudes of the two terms are equal. The ideal case is when $\epsilon = 0.5$ and $\phi = 0, \pm\pi, ...,$ which corresponds to two of the maximally entangled Bell states. For polarization entanglement, we can take $|0\rangle = |V\rangle$ and $|1\rangle = |H\rangle$. To have high-quality entanglement, the source must be configured to avoid distinguishing information arising from correlations with other degrees of freedom, such as photon frequency or arrival time. For example, many sources based on birefringent nonlinear crystals utilize a temporal walk-off compensation crystal [11, 12, 15, 16] to avoid distinguishability due to arrival time. When using entangled photons from different sources or from spectrally filtered sources, it is critical to avoid frequency or spectral correlations that may reveal distinguishing information [17, 18].

Design of ultrafast sources of entangled photons often involves consideration of possible spectral correlations. Spectral correlations are most easily understood in terms of the joint spectral intensity (JSI) of the down-converted photons. The JSI is a plot of the SPDC intensity as a function of the signal and idler frequencies. It is the product of the pump-envelope function and the phase-matching function [17]. A perfectly uncorrelated source has JSI that is factorizable into two components that depend on the signal or idler frequency alone; namely, JSI $\propto p_s(\omega_s)p_i(\omega_i)$, where $p_s(\omega_s)$ ($p_i(\omega_i)$) is the probability that the signal (idler) photon has frequency ω_s (ω_i) in the JSI. When plotted in the $\omega_s - \omega_i$ plane, the pump-envelope function has an angle of $-45°$ to the ω_s-axis (because by energy conservation, $\omega_i = \omega_p - \omega_s$). An uncorrelated SPDC source with a factorizable JSI is desirable because correlations between the signal and idler are eliminated, thus removing distinguishing information, which is particularly important when entangling photons from different sources [17]. To achieve a factorizable JSI, the phase-matching function therefore needs to have an angle, $\alpha_{\text{PM}} \in [0°, 90°]$ to the ω_s-axis [18]. Type-2 downconversion in beta-barium borate (BBO) or KTiOPO_4 (KTP) are examples of SPDC processes in crystals that have appropriate phase-matching angle, α_{PM}, to achieve factorizable JSI (while LiNbO_3 does not offer $\alpha_{\text{PM}} \in [0°, 90°]$) [18]. Another consideration is that the pump bandwidth should be comparable to the SPDC bandwidth to get the factorizable, circular-shaped JSI [17]. For type-2 SPDC in KTP with pump near 775 nm and SPDC near 1550 nm, ps-duration pumping requires crystal lengths on the order of tens of millimeters, while 100 fs-duration pump requires crystals that are several millimeters in length.

To produce the entangled quantum state shown in Eq. 1, there needs to be two downconversion paths corresponding to the two terms. There have been several "two-path" SPDC schemes demonstrated, including use of two counter-propagating paths in a Sagnac interferometer [8, 19], two spatially separated paths in the same crystal [6, 9, 10, 19] and two consecutive SPDC crystals [7, 12, 16, 19]. Similar to two consecutive crystals, the two-paths can be formed by two consecutive sections in the same crystal with different quasi-phasematching periods [11, 20, 21] or two different QPM orders in a single-period grating [22, 23]. Here we study aperiodically poled KTP (aPPKTP) that is designed to simultaneously phasematch two SPDC processes using the phase-modulation domain-engineering technique.

The phase-modulation technique used to generate entangled-photons has previously been explored theoretically [24, 25] and experimentally in aperiodically poled LiNbO_3 [26–29] and in aPPKTP [30]. The phase-modulated domain design is related to dual-periodically poling [24, 25, 29]. Recently, domain-engineered aPPKTP was used to demonstrate polarization entangled photons [31] where the domain-engineering was based on nonlinear optical holograms [32, 33]. It is desireable to perform dual-process SPDC in a single crystal because it requires fewer external components, potentially reducing system complexity, improving phase stability, and minimizing optical losses.

In this work, we present a detailed exploration of dual-process SPDC based on the phase-modulated domain-engineering technique in aPPKTP. One feature of dual-process SPDC using the phase-modulation technique is that the phase ϕ in Eq. 1 is fixed during fabrication. With type-2 SPDC in aPPKTP, where the signal and idler are orthogonally polarized and pumped by the same polarization, it is difficult to adjust ϕ because it is hard to separate the two components in Eq. 1. We study how the phase ϕ affects the SPDC output, and we show how high polarization-entanglement visibility can be obtained using a new technique where quarter-wave plates are placed in the signal and idler paths. This work serves as a guide on how to practically implement polarization-entangled photon-pair generation in phase-modulated domain-engineered crystals. Using our scheme, average polarization entanglement visibility over 0.98 was demonstrated in aPPKTP.

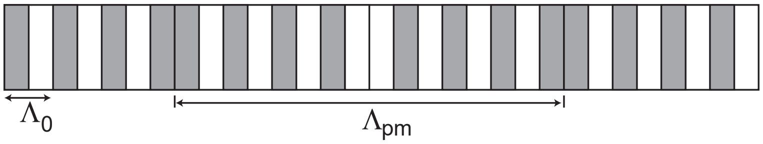

Fig. 1. Example of a phase-modulated QPM structure with fundamental period, Λ_0 and phase-modulation period, $\Lambda_{\rm pm}$.

2. Phase-modulated poling design

Phase-modulated domain-engineering is part of the broader technique of quasi-phasematching (QPM) [34], where the sign of the nonlinear coefficient is periodically modulated. In $LiNbO_3$ and KTP, this periodic modulation is achieved through ferroelectric domain poling. For SPDC in a uniform quasi-phasematched crystal, the downconversion spectrum is a function of the phase-mismatch, Δk, which is described by

$$I_{\rm SPDC} \propto {\rm sinc}^2\left(\frac{\Delta k L}{2}\right), \tag{2}$$

where $I_{\rm SPDC}$ is the SPDC intensity, L is the crystal length, ${\rm sinc}(x) = \sin(x)/x$ and

$$\Delta k = k_p - k_s - k_i \pm \frac{2\pi}{\Lambda_0}. \tag{3}$$

The wavevector, k_j, is given by $2\pi n_j/\lambda_j$, where n_j is refractive index at the wavelength λ_j ($j = p, s, i$ represent the pump, signal and idler, respectively). Λ_0 is the QPM period of the crystal. The poled nonlinear crystal effectively forms a standing-wave modulation in the nonlinear coefficient, which means that in Eq. 3, the term containing the QPM contribution, $2\pi/\Lambda_0$, can have sign +1 or -1. This implies that the same QPM grating can compensate for both ($k_p > k_s + k_i$) or ($k_p < k_s + k_i$).

Phase-modulated domain engineering involves modifying the sequence of periodically poled domains [28, 35, 36]. Starting with the fundamental QPM period, Λ_0, the phase in each QPM period is modified, and the periodicity of the phase-modulation pattern is given by $\Lambda_{\rm pm}$ (see Fig. 1). The phase-modulated poling structure can phasematch multiple simultaneous processes at

$$\Delta k_m = 2\pi\left(\pm\frac{1}{\Lambda_0} + \frac{m}{\Lambda_{pm}}\right). \tag{4}$$

Compared to [35, 36], Eq. 4 differs in that the sign of Λ_0 can be ± 1 because of the same arguments for $\pm\Lambda_0$ in Eq. 3 discussed above.

For type-2 downconversion in KTP at 775 nm ⟶ 1530.7 nm + 1569.8 nm, we take

$$\begin{aligned} \Delta k_{+1} &= 2\pi\left(\frac{n_{p,o}}{\lambda_p} - \frac{n_{s,o}}{\lambda_s} - \frac{n_{i,e}}{\lambda_i}\right) \\ \Delta k_{-1} &= 2\pi\left(\frac{n_{p,o}}{\lambda_p} - \frac{n_{s,e}}{\lambda_s} - \frac{n_{i,o}}{\lambda_i}\right), \end{aligned} \tag{5}$$

where o and e represent ordinary and extraordinary polarizations, respectively. Combining Eqs. 4 and 5 and using KTP dispersion relations from [37, 38] with temperature dependence from [39], we theoretically predict matched wavelengths between the $o \rightarrow oe$ and $o \rightarrow eo$ processes to occur at temperature 42.2 °C with $\Lambda_0 = 46.155\ \mu$m and $\Lambda_{pm} = 1.385$ mm. In our experiment, o corresponds to the H-polarization and e to the V-polarization. The SPDC wavelengths are chosen to be far enough apart for easy spectral separation and close enough together so that the

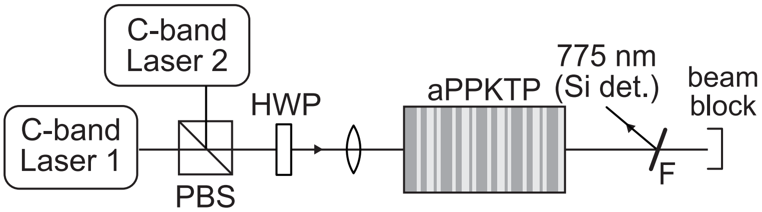

Fig. 2. SFG experimental setup. The SFG spectrum is measured by fixing laser 2 (V-polarized) and scanning the wavelength of laser 1 (H-polarized) while measuring the generated sum frequency (SF) light near 775 nm using a silicon detector preceded by a dichroic filter, F. The HWP is set at 0° (original polarizations) or 22.5° (laser polarizations rotated by 45°). PBS, polarizing beam splitter; HWP, half-wave plate

bandwidths of the two SPDC processes are nearly matched. Large detunings between the signal and idler can lead to bandwidth mismatch and loss of indistinguishability between the two downconversion paths [22].

3. Experimental Characterization Using Sum-frequency Generation

A set of aperiodically poled KTP crystals based on the designs discussed in Section 2 was fabricated and then tested using sum-frequency generation (SFG). The SFG measurement setup is shown in Figure 2, where two continuous-wave, orthogonally polarized, C-band lasers are combined on a polarizing beam splitter (PBS) and sent to the aPPKTP crystal. The wavelength of laser 1 is scanned while the wavelength of laser 2 is fixed. We recorded the generated optical power near 775 nm using a silicon detector, which is H-polarized due to phasematching. A half-wave plate (HWP) is placed after the PBS. Using the HWP, we can vary the incident polarization states such that the two C-band probe lasers are polarized along the principle axes of the aPPKTP crystal, or to rotate both probe-laser polarizations by 45° so that both type-2 SFG processes can be observed at the same time.

Using the SFG measurement setup, we first characterized the relative peak heights of the two frequency conversion processes and conversion wavelengths for several aPPKTP crystals. According to Section 2, for the dual-process domain-engineered crystals, the choice of conversion wavelengths (in this case, 775 nm → 1530.7 nm + 1569.8 nm) determines the fundamental QPM period, Λ_0 and the phase-modulation period, Λ_{pm}. The specific choice of phase-modulation function, $\phi(z/\Lambda_{\mathrm{pm}})$, determines the relative strengths of the two conversion processes (that is, the relative heights of the two peaks in the SF spectrum) [28]. We selected four phase-modulation functions close to, but not exactly the same as the 50:50 function [28] with different expected relative peak heights. The four aPPKTP crystals were designed to have peak ratios of 1.00, 0.96, 1.05 and 1.10, where the peak ratio is defined as the ratio between the o-polarized (H-polarized) peak near 1530 nm to the peak with the same polarization near 1569 nm. Examining the wavelengths, we experimentally confirmed that the SFG wavelengths for all four crystals were the same and within 0.5 nm of the theoretical design wavelengths. For the peak-height ratios, results of comparing the measured and theoretically predicted ratios are shown in Table 1. We see that there is good agreement for all four of the aPPKTP crystal designs.

Figure 3 shows SFG results of a 30 mm long aPPKTP crystal with phase-modulated poling pattern designed for equal amplitudes of the two nonlinear-optical processes. In Fig. 3a, laser 2 (V-polarized) is fixed to 1530.5 nm or 1569.2 nm and laser 1 (H-polarized) is scanned. The crystal temperature was 45 °C and the HWP is at 0° (effectively removed). We observe equal amplitude of the two SFG processes, which is in agreement with the design.

In Fig. 3b, we investigate temperature tuning of SFG with laser 2 is fixed at 1530.5 nm. In this

Table 1. Comparison of Theoretical and Measured Peak-height Ratios

Grating design	Peak ratio (theory)	Peak ratio (measured)
A	1.000	1.001
B	0.962	0.939
C	1.053	1.034
D	1.097	1.101

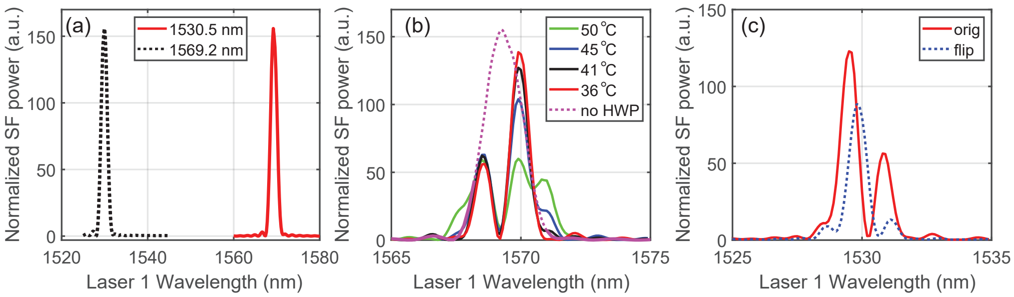

Fig. 3. SFG experimental results. (a) Normalized detected SF power (at 775 nm) with the HWP at 0° (laser 2 at 1530.5 nm or 1569.2 nm). (b) With HWP rotating input lasers by 45°, SF output at different temperatures (laser 2 fixed at 1530.5 nm). The spectrum with no HWP rotation shown for comparison. (c) At 36 °C and laser 2 at 1569.2 nm, SF spectra comparison for original crystal orientation and flipped crystal.

measurement, the HWP is set to 22.5° and used to rotate both probe-laser polarizations by 45° so that both SFG processes are observed at the same time. Using this configuration, we observe interference between the two SF processes, manifested as a fringe pattern. For comparison, the detected SF output is plotted with the HWP at 0° (so that the HWP is effectively removed and only one SF process is present), and we see a broad peak without interference fringes. The observed fringe pattern is quite stable as the crystal temperature is tuned, which we believe is because the relative phase between the two processes (corresponding to ϕ in Eq. 1) is constant, fixed by the phase-modulation pattern of the crystal and unchanged by crystal temperature.

To investigate this interference effect further, we measured the SF spectra with HWP at 22.5° and the aPPKTP crystal flipped (so that the exit face becomes the input face). By flipping the crystal, the specific poling pattern encountered by the light is changed, thereby changing the relative phase ϕ in Eq. 1. Figure 3c compares SF spectra (with laser 2 wavelength at 1569.2 nm) for the original and flipped aPPKTP orientation of the same crystal. The HWP was set to 22.5° to reveal the interference pattern. The crystal temperature was 36 °C. In the flipped orientation, the fringe pattern changes, indicating a different phase factor ϕ between the two frequency-conversion processes. The periodicity of the fringes is the same, but the fringes appear shifted compared to the measurement using the original orientation. We also note that the SF spectrum for the original orientation is the mirror of the spectrum measured in Fig. 3b, where laser 2 is at 1530.5 nm, which follows from swapping short- and long-wavelength lasers.

These measurements confirm that the relative phase ϕ between the two frequency-conversion processes for these aPPKTP crystals is fixed during fabrication. The exact value of ϕ is not known and depends on the specific domain pattern, as illustrated in the SFG comparison of the flipped vs. original orientations (Fig. 3c). In Appendix A, we describe a procedure for compensating for effects of non-zero ϕ to improve the polarization-entanglement visibility.

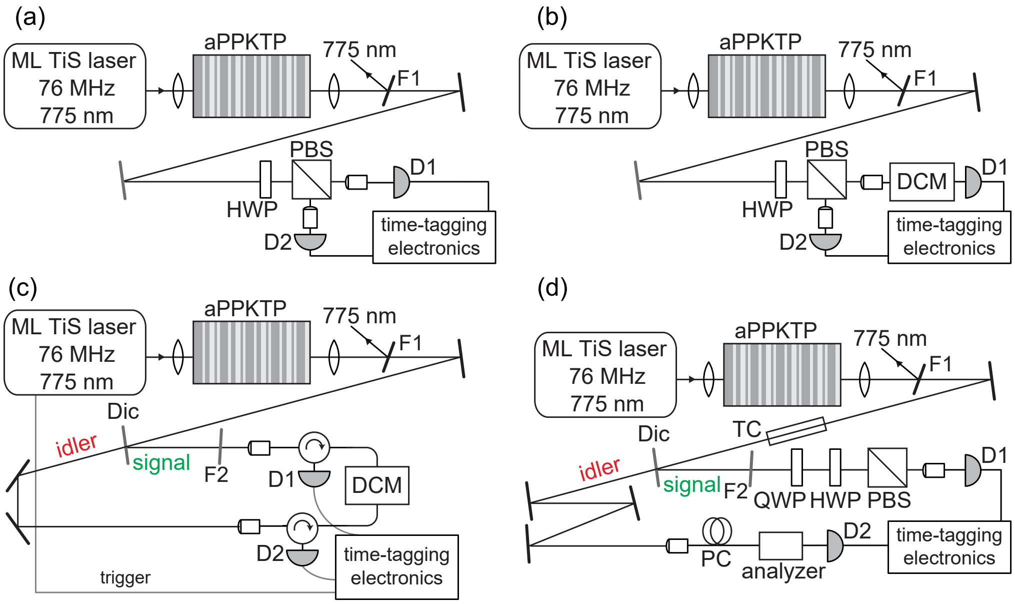

Fig. 4. Summary of SPDC experimental setups. (a) Measurement of SPDC collection and generation efficiency. (b) Single-DCM time-of-flight spectroscopy measurement. (c) Time-of-flight measurement for observing the joint spectral intensity. (d) Polarization entanglement measurement. PBS, polarizing beam splitter; HWP, half-wave plate; QWP, quarter-wave plate; DCM, dispersion compensation module; Dic, dichroic mirror; F1, pump rejection filter; F2, 10 nm bandpass filter centered at 1530 nm; TC, temporal walk-off compensation crystal; PC, fiber-based polarization controller; D1(2), single-photon detector.

4. SPDC Characterization

We characterized SPDC using the 30-mm-long aPPKTP crystal designed for equal amplitudes of the two frequency conversion processes. The experimental setups for the different measurements are summarized in Fig. 4. Common to all setups, a 1.6 ps duration, 76 MHz mode-locked (ML) Ti:Sapphire laser at 775 nm was focused to a beam waist of 120 μm. A lens is placed after the aPPKTP crystal. Using 1550-nm light back-propagated from the collection fibers to the crystal, we arranged for 65 μm collection beam waist. The crystal was AR-coated for the pump at the input surface and AR-coated for the SPDC wavelengths at the output surface. The downconverted photons were detected with two super-conducting nanowire single-photon detectors (SNSPDs), represented by D1 and D2 in Fig. 4. Various components (polarizing beam splitters, filters, etc.) are placed in the output path to perform different characterization measurements.

4.1. Entangled-Photon-Pair Generation

Using the setup in Fig. 4a, we measured the SPDC collection and generation efficiencies. The pump beam was focused loosely compared to the SPDC collection beam waist, as described above. We use a polarizing beam splitter (PBS) to separate and direct the SPDC output to the two SNSPDs, labeled D1 and D2. Using 51 mW average pump power, we observed coincidence count rate between detectors D1 and D2 of 6.05×10^3 counts/s, and singles counts rates of 2.70×10^4 counts/s and 2.00×10^4 counts/s at D1 and D2, respectively. Using previously measured detection efficiencies for D1 and D2 of 88% and 93%, respectively, and the measured coincidence and singles count rates, we estimated the collection efficiency [40] of the D1 (D2) arm to be 34%

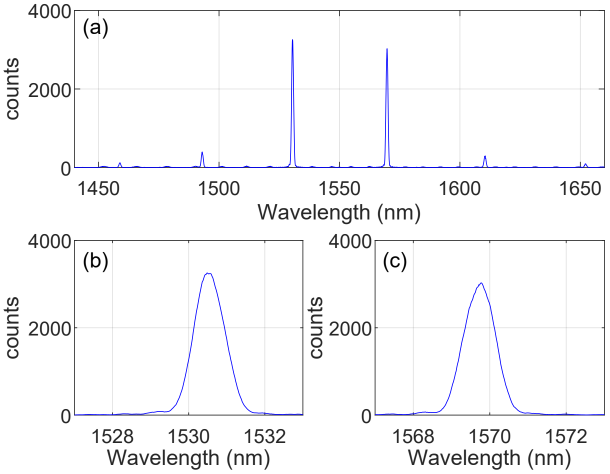

Fig. 5. ToF SPDC spectra. (a) Full scan, and zoom in of (b) signal and (c) idler peaks. The wavelength is for the H-polarized photon, the counts are integrated over 3 minutes, the time-bin size is 32 ps (or 0.02 nm bin size), and the crystal temperature is 45 °C.

(24%). The dark count rate for each of the two SNSPDs was $\approx$ 100 counts/s, which is sufficiently low to be neglected in these calculations. From these measurements, we estimated the internal pair-production generation efficiency of 1.4×10^4 pairs/s/mW.

4.2. SPDC Spectral Measurements

We used time-of-flight (ToF) spectroscopy [41, 42] to characterize the SPDC spectra. ToF spectroscopy uses a dispersive medium to translate spectral variations into arrival-time variations at the detector. In this work, the dispersive medium was a fiber dispersion compensation module (DCM) providing approximately 1.6 ns/nm dispersion. For this measurement and subsequent measurements, we used a different set of SNSPDs than those used in Section 4.1. These detectors had lower timing jitter around 150 ps with lower detection efficiency (around 65% rather than $>$ 85%) and dark count rates between (500 to 1000) counts/s. We estimate the total jitter from the SNSPDs and time-tagging electronics to be 0.16 ns full-width at half maximum, which translates to 0.1 nm spectral resolution from the DCM dispersion. The experimental setup for the ToF measurement is shown in Fig. 4b. One of the outputs of the PBS is sent directly to detector D2 (forming the “start” pulse), while the other output is sent to the DCM then detector D1 (“stop” pulse). A HWP is placed before the PBS to swap the H- and V-polarizations as the start and stop pulse, or to send components of both H- and V-polarizations to both outputs of the PBS. This latter configuration allowed us to determine the crystal temperature where the wavelengths of the two SPDC processes are matched, and also aided in ToF wavelength calibration [27].

Figure 5 plots the result of the ToF measurement with the HWP arranged so that the H-polarized photons are sent to the DCM and dispersed, while the V-polarized photons form the start pulse. The crystal temperature was 45 °C where the two downconversion processes have closely matched wavelength with signal at 1530.5 nm and idler at 1569.8 nm. The ToF spectral measurement also showed two pairs of farther-spaced peaks in the SPDC spectrum, which arise from accidental phasematching from the phase-modulated grating design [28]. For entanglement measurements, these peaks must be filtered out because they represent photons uncorrelated with the desired photon pair at 1530.5 nm and 1569.8 nm (namely, these other photons contribute to accidental coincidences). For this reason, in the experimental setups illustrated in Figs. 4c and d, we place a 10 nm bandpass filter centered at 1530 nm in the signal arm of the measurement setup, which is

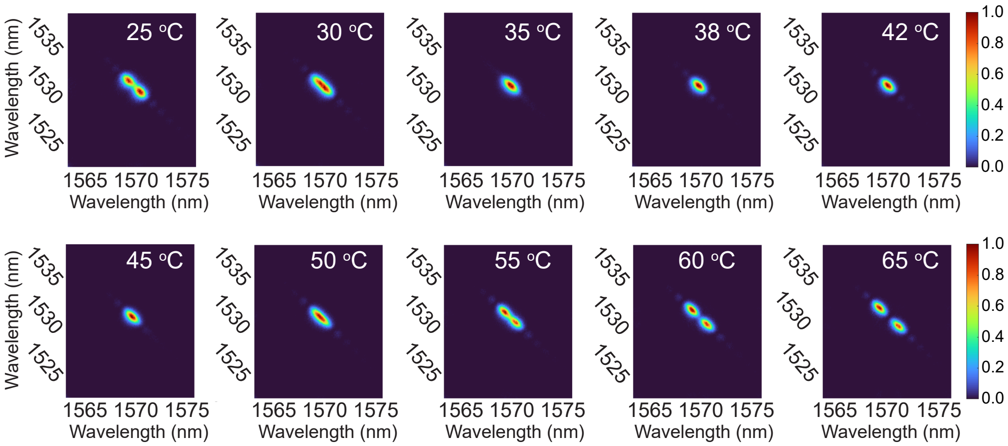

Fig. 6. Temperature tuning of the JSI. The idler wavelength is plotted along the x-axis, the signal is along the y-axis, and the color bar shows relative intensity. Each measurement was taken with integration time of 4 minutes and 0.1 ns bin size (about 0.06 nm spectral width).

sufficient to suppress coincidences arising from the accidentally phasematched peaks.

4.3. Measurement of the Joint Spectral Intensity

Figure 4c shows the setup for measuring the joint spectral intensity for the SPDC. Instead of separating by polarization, a dichroic mirror is used to separate the signal near 1530 nm from the idler near 1570 nm. The dichroic mirror is placed at near-normal incidence to minimize polarization dependent loss. Both signal and idler are dispersed by the DCM. We use a pair of circulators to send the signal and idler in opposite directions through the same DCM. As mentioned above, we placed a bandpass filter (at 1530 nm, 10 nm bandwidth) in the signal arm to reject SPDC photons arising from the accidentally phasematched processes.

Figure 6 plots JSI measurements as a function of temperature with the idler (signal) wavelength along the x-axis (y-axis). At low temperatures around $T = 25\,^\circ\mathrm{C}$, two spots are visible in the JSI, which correspond to the $|HV\rangle$ and $|VH\rangle$ downconversion states. From temperature tuning, we identify the $|VH\rangle$ ($|HV\rangle$) state as the lower-right (upper-left) spot in the $T = 25^\circ$ JSI. As the temperature increases, the spots merge, indicating that their wavelengths become matched and wavelength distinguishability is removed. It is at this temperature where we obtain the polarization-entangled state. Further increases in temperature cause separation of the spots and produce wavelength distinguishability.

These JSI measurements tell us several things. Firstly, the JSI measurements show near equal amplitude of the $|HV\rangle$ and $|VH\rangle$ states, matching the design and the SFG characterization. It also confirms that the JSI measurement setup (Fig. 4c) does not add significant polarization-dependent loss to the detected state. Secondly, the temperature where the wavelength degeneracy is established is found to be near $T = 42\,^\circ\mathrm{C}$. At this temperature, the JSI is a tight, single spot and almost circular in shape, which indicates that the pump bandwidth is a close match to the SPDC bandwidth. In our experiment, we use a 1.6 ps duration, 775-nm wavelength modelocked Ti:sapphire laser pump (with spectral bandwidth of 0.35 nm or 5.9 cm^{-1}) and type-2 downconversion near 1550 nm in a 30-mm long aPPKTP crystal (with SPDC bandwidth of 1.0 nm or 4.2 cm^{-1}). The circular-shaped JSI is desirable because it indicates that distinguishing spectral correlations are minimal. Upon close inspection of the JSI, the sinc^2 sidelobes of the SPDC can be seen, but these are quite small in amplitude compared to the main peak.

4.4. Polarization-Entanglement Measurements

Figure 4d shows the setup for measuring polarization entanglement. The SPDC photons are sent through a temporal walk-off compensation crystal (marked "TC" in the diagram) that compensates for the temporal walkoff caused by birefringence in the aPPKTP crystal [15]. The TC consists of an unpoled KTP crystal, with length half that of the aPPKTP crystal, rotated by 90° so that the fast and slow birefringence axes are swapped compared to the aPPKTP crystal. Here, the TC was 15 mm long to go with the 30-mm-long aPPKTP crystal. After the TC, the SPDC photons are separated into signal and idler arms using a dichroic mirror placed at near-normal incidence. We used a manually-controlled, free-space QWP-HWP-polarizer combination in the signal arm and a computer-controlled, fiber-based QWP-HWP-polarizer combination (labeled "analyzer") in the idler arm. Because the analyzer had non-polarization-maintaining (non-PM) fiber input and output, we used a fiber-based polarization controller (PC) to adjust the polarization incident on the analyzer. With the free-space QWP-HWP-polarizer combination in the signal arm, the angles of the signal QWP and HWP relative to the H- and V-polarization orientation were clear. However, with the non-PM fiber and PC, the angles of the QWP and HWP in the idler arm were less clearly determined. Ideally, the analyzers in the signal and idler arms should have been matched, but we were limited by equipment availability.

We optimized the polarization-entanglement fringes in a three-step process. In the first step, we set the aPPKTP crystal temperature to 42 °C, and we maximized the collection efficiency. Next, we set the signal QWP angle to zero (that is, having the principal axes aligned parallel to the H- and V-polarizations of the crystal) and the idler QWP angle to zero according to the controller. We then adjusted the PC to obtain high visibility for the two polarization-entanglement fringes where $\theta^s_{\mathrm{HWP}} = 0°$ and 45°. Operationally, this meant we looked for minimum coincidences for output states $|HH\rangle$ and $|VV\rangle$. An example of results of this step is shown in the Appendix (Fig. 9a). In the third step, both signal and idler QWP angles were rotated by 45° relative to the second step, and small adjustments to the PC were performed to maximize visibility of all four polarization fringes (example of which is shown in Fig. 9b). The theory behind the 45° QWP rotations is described in Appendix A. In essence, the action of the QWP rotation is to compensate for non-idealities in the entangled photon state caused by unequal peak amplitude and the relative phase ϕ. In the adjustment process, we allowed some very small adjustments (±5°) to the two QWPs and two HWPs owing to uncertainty in the waveplate placement in the holders. More detailed about this alignment and optimization process are discussed in the Appendix A.3.

We measured the polarization-entanglement fringes from the aPPKTP crystal as a function of temperature. After first optimizing the polarization entanglement near 44 °C, we varied the aPPKTP temperature from 25 °C to 60 °C. Figure 7 shows the temperature tuning of the polarization fringes. In these measurements, the visibility of the fringes decreases as the crystal temperature deviates from the optimal temperature near 44 °C. The average incident pump power incident was 44 mW, and the integration time for each coincidence measurement was 2 seconds.

In Table 2, we the list the visibility for each of the four cases, $\theta^s_{\mathrm{HWP}} = 0°, 45°, 22.5°$ and $-22.5°$ for the results at $T = 44\,°\mathrm{C}$ (Fig. 7c). The visibility is defined as $(N_{\max} - N_{\min})/(N_{\max} + N_{\min})$, where $N_{\max}$ and $N_{\min}$ are the maximum and minimum number of coincidences obtained from sinusoidal curves fitted to the data. The uncertainty in visibility is estimated from the 95% confidence interval of the fit. Based on these four visibilities, the average visibility for the case at $T = 44\,°\mathrm{C}$ is 0.984 ± 0.003. Furthermore, the Clauser–Horne–Shimony–Holt (CHSH) parameter, S [19, 43, 44], calculated from this data is $S = 2.801 \pm 0.014$, where we have taken $\alpha = 0°$, $\alpha' = 45°$, $\beta = 154.5°$ and $\beta' = 109.5°$. This S value significantly violates Bell's inequality and indicates a highly non-classical state. With this high polarization-fringe visibility and high S value, we argue that an entangled-photon pair source based on aPPKTP is a useful, high-quality pair source for quantum networking and other applications.

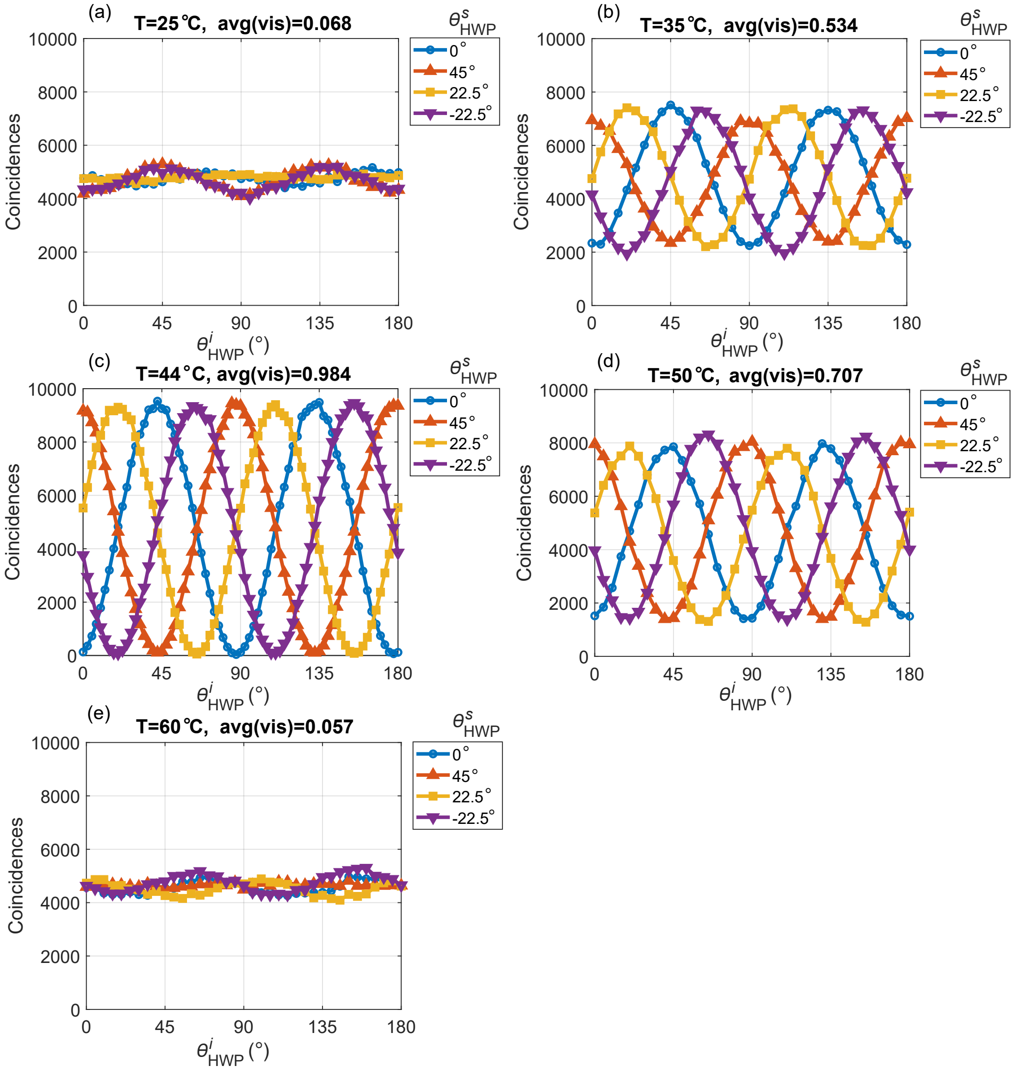

Fig. 7. Polarization-entanglement fringes measured with 2 s integration time per step at different aPPKTP temperatures: (a) 25 °C, (b) 35 °C, (c) 44 °C, (d) 50 °C, (e) 60 °C.

5. Discussion

Domain-engineered, aperiodically poled nonlinear crystals like aPPKTP are attractive for SPDC because they offer high-quality entanglement in a single crystal. They are simpler to align compared to Sagnac [8] or two-path [9,10] SPDC schemes. There are several different techniques to achieve dual-process downconversion in a single crystal for generation of polarization-entangled photon pairs. These techniques include the phase-modulation technique (presented here), use of two consecutive QPM periods [11,20,21], or two different QPM orders [22,23] and the nonlinear optical hologram technique [31–33].

For the same total crystal length and combination of wavelengths, numerical calculations showed that dual-process downconversion using the phase-modulation technique has both half as narrow bandwidth and higher conversion efficiency compared to using two consecutive QPM periods [28]. In essence, the two SPDC processes are generated in a distributed fashion

Table 2. Visibility extracted from the measured polarization fringes at $T = 44\,^\circ\mathrm{C}$

θ^s_{HWP}	signal polarization	Visibility
0°	$\lvert H\rangle$	0.987 ± 0.007
45°	$\lvert V\rangle$	0.982 ± 0.005
22.5°	$\lvert D\rangle$	0.983 ± 0.006
-22.5°	$\lvert A\rangle$	0.983 ± 0.007

throughout the phase-modulated crystal, thus utilizing the full length, while for the case of two consecutive periods, each SPDC process is limited to only half the crystal. Generally speaking, longer crystals (greater than several cm) are more difficult to fabricate so the phase-modulation domain-engineering technique can be useful for obtaining narrower SPDC bandwidths.

Using two different QPM orders to simultaneously phasematch two SPDC processes requires only a uniform periodically poled grating. However, the wavelengths where the two SPDC processes become matched in wavelengths can not be freely chosen but must be found using phasematching calculations. Ref. [22] studied type-2 SPDC in PPKTP with the +1 and -1 QPM orders, which have matched effective nonlinear coefficients, but the dispersion of KTP dictates that matched SPDC wavelengths can only be achieved for pump wavelengths between approximately 420 nm and 540 nm. Furthermore, near degenerate signal and idler wavelengths (needed for matched SPDC bandwidths) can only be achieved with the pump wavelength near 465 nm and SPDC wavelengths near 930 nm, far from the 1550 nm wavelengths compatible with optical fibers. For the experimental wavelengths used in Ref. [22] of 532.3 nm $\longrightarrow$ 904.3 nm + 1293.9 nm, the large signal and idler detuning resulted in mismatched bandwidths of the two SPDC processes, and a filter was needed to produce indistinguishability, resulting in higher losses. In another work [23], matched wavelengths in a PPKTP waveguide were obtained for the first QPM order using the d_{24} nonlinear coefficient and the third QPM order using the d_{33} coefficient, which resulted in the conversion efficiency of one SPDC process being about 4.5 times larger than the other SPDC process. Waveguide engineering allows somewhat greater flexibility in the choice of wavelengths, but it is not clear from Ref. [23] how one would use simultaneous type-0 and type-2 SPDC to construct a polarization-entangled state.

Recently, the nonlinear-optical-hologram technique [31–33] was used to achieve domain-engineered SPDC in aPPKTP. Using this domain-engineering technique, Ref. [31] reported high-quality polarization entanglement and a relative phase of π between the two SPDC processes. Also, they reported that the 4 mm long aPPKTP crystal generated signal and idler at 1548 nm and 1572 nm, respectively, with 13 nm SPDC bandwidth (equal to 54 cm^{-1}). This SPDC bandwidth is similar to the bandwidth if two consecutive, 2 mm long QPM gratings were used, but it is not clear whether the wide bandwidth was intentionally designed or a limitation of the nonlinear-optical-hologram technique. The pump laser for their experiment was listed at 780 nm wavelength with 7 nm bandwidth (equal to 115 cm^{-1}), which would have corresponded to a non-circular JSI, contrasting with their measured result. Ref. [31] also noted that the fiber add-drop filter used to spectrally separate the signal and idler introduced an unknown amount of relative phase between the two SPDC processes (due to twist birefringence) that they compensated using a tilted QWP. The density matrix measurement was performed after the spectral filter so it is not clear whether the SPDC crystal produced π relative phase shift (or π with some small offset). If the relative phase shift between the two SPDC processes is not equal to π, then the procedure presented in our work here can be applied as a correction. In terms of the S parameter that characterizes the degree to which Bell's inequality is violated, our aPPKTP-based SPDC source showed a slightly higher value with $S = 2.801 \pm 0.014$ while the source in Ref. [31] had $S = 2.747 \pm 0.004$. The results presented in Ref. [31] appear highly promising, but details of the nonlinear-optical-hologram design procedure were not readily apparent.

We believe that the phase-modulation domain-engineering technique is an attractive solution for dual-process SPDC. The SPDC wavelengths can be chosen to be in the telecommunications band to match the low-loss wavelengths for optical fibers and to be compatible with existing telecom fiber components. After filtering accidentally phasematched SPDC peaks and applying compensation to correct for the relative phase between the two SPDC processes, high-quality polarization entanglement can be obtained (both high polarization-entanglement-fringe visibility and large S parameter) using these crystals.

6. Conclusion

We have fabricated aPPKTP crystals based on the phase-modulation domain-engineering technique and successfully used these crystals for polarization-entangled photon-pair generation. We obtained high quality polarization-entanglement, as seen in the polarization-entanglement fringes that exhibited average visibility equal to 0.984 ± 0.003 with CHSH S-parameter equal to 2.801 ± 0.014. Spectral measurements showed high-quality fabrication with results that matched the theoretical sinc^2 curves and theoretical peak-height ratios. Using a ps-duration pump laser, we showed nearly round JSI.

One drawback of these crystals is that the relative phase and amplitude ratio between the two SPDC processes are fixed during fabrication and may be non-ideal. We present a new method to compensate for these effects to obtain high polarization fringe visibility with high CHSH S parameter. The procedure uses quarter-wave plates placed in the signal and idler arms. This procedure can be applied to other SPDC sources where ϵ and ϕ are poorly controlled due to generation or due to polarization-dependent optics after the SPDC source.

Domain-engineered, aperiodically poled SPDC crystals are attractive for their robustness and simplicity, which are properties that are of interest for sources in real-world quantum networks, in integrated photonics and in space-based quantum communications. SPDC using aperiodically poled crystals or waveguides can be a route towards a compact, robust and scalable platform for producing photonic qubits. Using the phase-modulation domain-engineering technique to achieve dual-process-SPDC for polarization-entangled photon generation is attractive because it is easy to implement, allows flexibility in wavelength and produces relatively narrow SPDC bandwidths. Applying the QWP compensation procedure presented here allows control of effects of relative phase between the two SPDC processes, which is a key advance that will allow practical, widespread deployment of phase-modulation domain-engineering aperiodically poled SPDC crystals in quantum networks and other applications.

A. Controlling effects of the relative phase and amplitude mismatch in entangled-photon states

In this Appendix, we present theory, modeling and experimental results of how effects of amplitude mismatch, $\epsilon \neq 0.5$, and the relative phase, ϕ, in Eq. 1 can be compensated using quarter-wave plates placed after the SPDC crystal. In previous work using other SPDC schemes, ϕ was controlled by the incident pump and its polarization [7,16] or by slightly tilting the SPDC crystal itself [7]. The phase, ϕ, can also be managed by using a Michelson interferometer after the SPDC, which also serves to provide temporal walk-off compensation [20]. In this Appendix, we discuss a different technique where quarter-wave plates are placed in the signal and idler paths to compensate for effects of ϵ and ϕ.

A.1. Theory

We can rewrite the entangled state Eq. 1 more explicitly as

$$\begin{aligned} |\Psi\rangle &= \sqrt{\epsilon}|10\rangle + e^{i\phi}\sqrt{1-\epsilon}|01\rangle \\ &= \sqrt{\epsilon}|H\rangle_s \otimes |V\rangle_i + e^{i\phi}\sqrt{1-\epsilon}|V\rangle_s \otimes |H\rangle_i \\ &= \sqrt{\epsilon}\begin{pmatrix}1\\0\end{pmatrix} \otimes \begin{pmatrix}0\\1\end{pmatrix} + e^{i\phi}\sqrt{1-\epsilon}\begin{pmatrix}0\\1\end{pmatrix} \otimes \begin{pmatrix}1\\0\end{pmatrix}, \end{aligned} \tag{6}$$

where the operator $\otimes$ represents the tensor product [45] between states at s and i. For clarity, $|1\rangle = |H\rangle$ and $|0\rangle = |V\rangle$, where H and V refer to horizontal and vertical polarizations, respectively.

To analyze the polarization entanglement, we place polarization analyzers at s and i. Each analyzer consists of a quarter-wave plate (QWP) followed by a half-wave plate (HWP), then linear polarizer and finally a single-photon detector. We can calculate the coincidences per trial between s and i as a function of the QWP and HWP angles by utilizing the Jones matrix calculus [46]. If θ is the angle of the waveplate's fast axis with respect to the horizontal polarization, then the Jones matrix for a HWP is [46,47]

$$\mathbf{J}_{\mathrm{HWP}}(\theta) = \begin{pmatrix} \cos 2\theta & \sin 2\theta \\ \sin 2\theta & -\cos 2\theta \end{pmatrix}, \tag{7}$$

and the Jones matrix for a QWP is [46,47]

$$\mathbf{J}_{\mathrm{QWP}}(\theta) = \begin{pmatrix} \cos^2\theta + i\sin^2\theta & (1-i)\cos\theta\sin\theta \\ (1-i)\cos\theta\sin\theta & \sin^2\theta + i\cos^2\theta \end{pmatrix}. \tag{8}$$

The Jones matrix of the waveplate combination, $\mathbf{J}_{\mathrm{WP}}$, is then

$$\mathbf{J}_{\mathrm{WP}}(\theta_h, \theta_q) = \mathbf{J}_{\mathrm{HWP}}(\theta_h)\mathbf{J}_{\mathrm{QWP}}(\theta_q). \tag{9}$$

The ordering of the matrices indicates that the QWP rotation is applied before the HWP rotation.

The output state after the waveplates is

$$|\Psi_{\mathrm{out}}\rangle = \mathbf{J}_{\mathrm{WP}}(\theta_h^s, \theta_q^s) \otimes \mathbf{J}_{\mathrm{WP}}(\theta_h^i, \theta_q^i)|\Psi\rangle, \tag{10}$$

where $|\Psi\rangle$ is given by Eq. 6. To calculate the coincidence probability per trial, we project $|\Psi_{\mathrm{out}}\rangle$ onto the detected state, which we take to be the horizontally polarized state,

$$|\Psi_{\mathrm{det}}\rangle = |H\rangle_s \otimes |H\rangle_i = \begin{pmatrix}1\\0\end{pmatrix} \otimes \begin{pmatrix}1\\0\end{pmatrix}, \tag{11}$$

such that

$$\text{probability of coincidence} = |\langle\Psi_{\mathrm{det}}|\Psi_{\mathrm{out}}\rangle|^2. \tag{12}$$

In this analysis, we take that the polarizers at both detectors to be horizontally oriented because the waveplate angles are defined relative to the H-polarization.

A.2. Modeling

In this section, we plot modeling results based on the theory in Sec. A.1. Fig. 8 shows calculated polarization-entanglement fringes for a few example cases. In each plot, we sweep the idler HWP angle from 0° to 180° with the signal HWP angle fixed at four settings: $\theta^s_{\mathrm{HWP}} = 0°, 45°, 22.5°, -22.5°$ that correspond to the horizontal, vertical, diagonal and anti-diagonal polarizations in the signal arm. In the left column of Fig. 8, both signal and idler QWP angles are set to 0°, while in the right column, both QWP angles are set to 45°, which produces a compensating effect that can significantly improve the quality of the polarization fringes. We note qualitatively similar results are obtained for QWP angles at −45°.

Figures 8a and b show the ideal entangled-photon case where $\epsilon = 0.5$, $\phi = 0$. The entanglement visibility, defined as $\mathrm{vis} = (\max - \min)/(\max + \min)$ is maximized at vis = 1 in both Figs. 8a and b. The effect of rotating both QWPs by 45° is to change the ordering of the fringes. More interesting effects are seen for cases where $\epsilon \neq 0.5$ and $\phi \neq 0$.

For non-ideally entangled states where either $\epsilon \neq 0.5$ or $\phi \neq 0$, without compensation, the polarization-entanglement fringes can have unequal height and can be unequally spaced in idler HWP angle, examples of which are shown in Figs. 8c, e, and g. By turning the signal and idler QWPs to 45°, the polarization fringes become equal in height and equally spaced (Figs. 8d, f, and h). In the second row of Fig. 8, $\epsilon = 0.5$ but non-zero ϕ causes reduced visibility (down to 0.707) for two out of the four polarization fringes. By rotating the QWPs to 45° (Fig. 8d), vis = 1 can be obtained for all four sets of polarization-entanglement fringes. In the third row, $\epsilon = 0.3$ and $\phi = \pi/4$. Without compensation using the QWPs, the entanglement visibility ranges from vis = 0.762 to 1 (0.881 average visibility), and after compensation, all four entanglement fringes have vis = 0.917. We also observe an offset in the idler HWP angle of the fringes that depends on ϕ in the polarization fringes after compensation. The last row of figure (Figs. 8g and h) shows the effect of increasing the relative phase, ϕ, compared to the the third row. With the QWP angles at 0°, there is degradation of the visibility, which ranges from 0.425 to 1 (0.713 average visibility). However, by applying the 45° rotation of both QWPs, the polarization fringes have equal spacing and equal visibilities, vis = 0.917.

To gain intuition on what is happening, let us examine the last two rows in Fig. 8. When $\epsilon < 0.5$, from Eq. 6 we see that the $|HV\rangle$ component is smaller than the $|VH\rangle$ component, which is confirmed in Figs. 8e and g where the amplitude of the curves for $\theta^s_{\mathrm{HWP}} = 45°$ (V-polarized signal) are larger than the curves for $\theta^s_{\mathrm{HWP}} = 0°$ (H-polarized signal). The maxima of these sets of curves occur at $\theta^i_{\mathrm{HWP}} = 0°, 90°$, etc. ($H$-polarized idler) for $\theta^s_{\mathrm{HWP}} = 45°$ (V-polarized signal), and at $\theta^i_{\mathrm{HWP}} = 45°, 135°$, etc. ($V$-polarized idler) for $\theta^s_{\mathrm{HWP}} = 0°$ (H-polarized signal). After rotating both QWPs by 45°, the four polarization fringes become equally spaced with equal amplitudes and an offset in θ^i_{HWP} proportional to ϕ. We believe the action of the 45°-oriented QWPs converts the light both arms into circular polarizations, and then measurement of the signal in a particular linear polarization state (defining each of the four fringes) projects the idler into a corresponding linear (or nearly linear) polarization state.

With this compensation procedure, namely turning both signal and idler QWP angles by 45°, there is a marked improvement in the polarization-entanglement fringes. The average visibility increases, and the four sets of polarization fringes become equal in amplitude. The degradation to the polarization fringes caused by $\phi \neq 0$ is removed. We see that the phase ϕ is proportional to an offset in the idler HWP angle (i.e., a fixed shift in the fringe patterns shown in Fig. 8). Also, we find empirically that fringe visibility after compensation only depends on the parameter ϵ and not ϕ. For example, we see this in comparing the top two cases where $\epsilon = 0.5$ and $\phi \neq 0$, and also the bottom two cases where $\epsilon = 0.3$ and ϕ differs.

This modeling supports the observation that the amplitude mismatch (i.e., $\epsilon \neq 0.5$) only weakly decreases the entanglement visibility, which was also shown in [48]. We see this in the examples for $\epsilon = 0.3$, which correspond to peak-height ratios of 0.429 (i.e., one peak is more than twice as

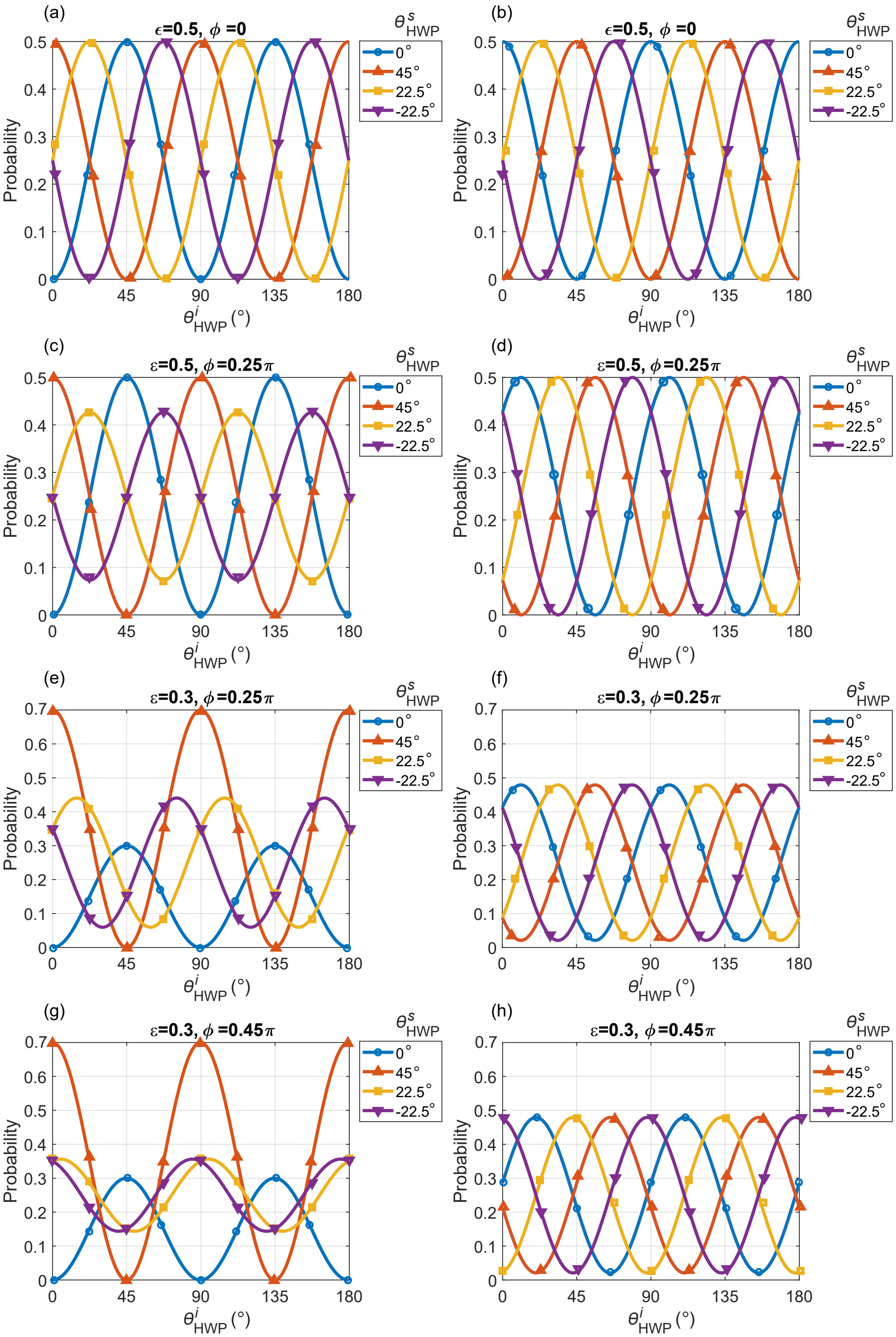

Fig. 8. Theoretical comparison of polarization-entanglement fringes (coincidence probabilities from Eq. 12) for various entangled states without (left column) and with (right column) compensation caused by $\theta^s_{\text{QWP}} = \theta^i_{\text{QWP}} = 45°$.

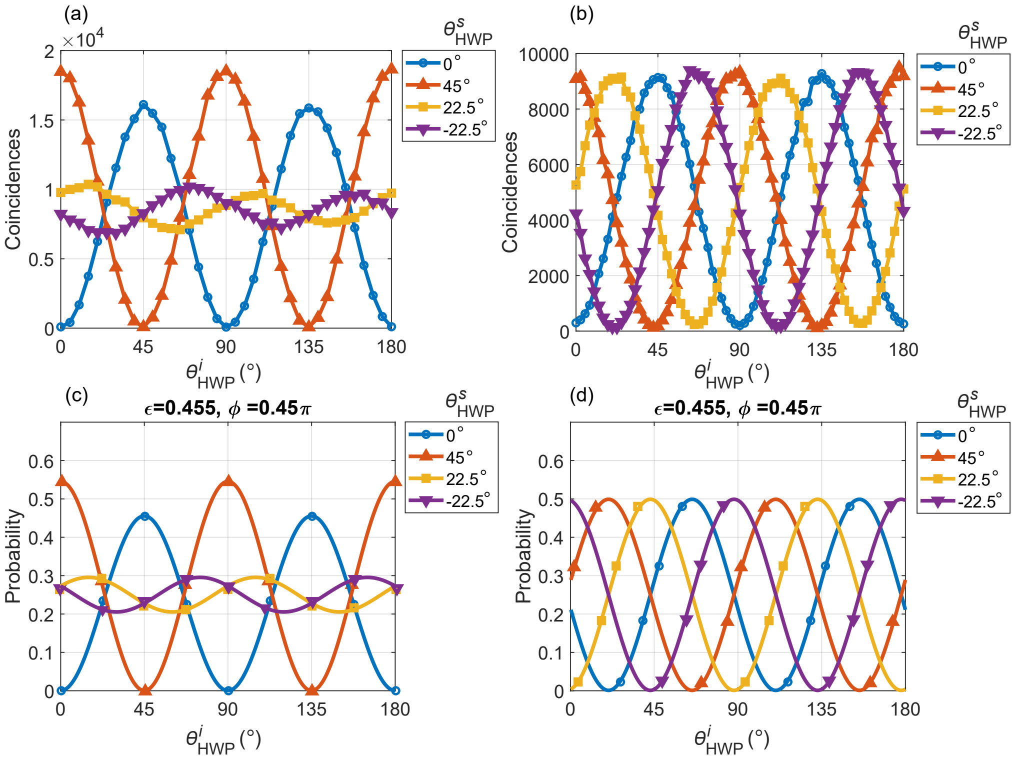

Fig. 9. Measured polarization-entanglement fringes (a) without and (b) with QWP compensation. The integration time for the coincidence measurements was 2 s, and the incident pump power was 75 mW in (a) and 39 mW in (b). Theoretical polarization fringes with $\epsilon = 0.455$ and $\phi = 0.45\pi$ (c) without and (d) with the QWP compensation.

tall at the other peak), where average visibilities of 0.917 can still be obtained after compensation. A corollary to this observation is that using the simple 50:50 phase-modulation domain pattern is sufficient rather than more complicated patterns [28] because the 50:50 pattern produces less than 5% deviation from equal peak heights (peak-height ratio = 1) [28]; effects of this amplitude mismatch will be negligible after applying the QWP compensation.

A.3. Experimental Example

Using the measurement setup shown in Fig. 4d, we optimized and measured the polarization-entanglement fringes. Figure 9a shows a set of polarization fringes where the QWP angles were at zero (that is, having the principal axes aligned parallel to the H- and V-polarizations of the crystal). The aPPKTP crystal temperature was set to 42 °C where the two SPDC processes are closely matched in wavelength. By adjusting the HWP angles and the fiber-based polarization controller, we were able to obtain high visibility for two of the four fringes. We attribute the poor visibility of the remaining two fringes to not having compensated for the relative phase ϕ in the SPDC state produced by the aPPKTP crystal. The polarization-entanglement visibility ranged from 0.147 to 0.994 with average visibility of 0.573.

In Fig. 9b, we turned both QWPs by 45° relative to the previous measurement and optimized the visibility. We obtained a marked improvement in all four polarization fringes. In this example, after compensation using the QWPs, the polarization-entanglement visibility ranged from 0.947 to 0.975 with average visibility of 0.961.

We used the theoretical model described in Section A.1 to calculate fringes that best approximated the results in Fig. 9a. Fig. 9c shows theoretical polarization-entanglement fringes for $\epsilon = 0.455$ and $\phi = 0.45\pi$ with signal and idler QWP angles set to zero, which show a strong resemblance to Fig. 9a. When the two QWPs are rotated by 45°, we obtain the fringes shown in Fig. 9d, where the visibility of all fringes becomes 0.996. We note that $\epsilon = 0.455$ corresponds to a peak-height ratio of 0.83, which is noticeably different that the ratio we measured for the aPPKTP using other experiments. We speculate that the measurement setup has a small amount of polarization dependent loss that affects the state arriving at the detectors.

We note that with our setup that used a fiber-based PC and analyzer with non-PM fiber in the idler arm, it is difficult to detect the offset angle in idler HWP predicted by our theory.

The effect of the QWP compensation can also be explored in terms of the S parameter [43,44]. Because the polarization-entangled fringes were measured at $\theta^s_{\mathrm{HWP}} = 0°, 45°, 22.5°$ and $-22.5°$, the signal's polarization angles were fixed to $\alpha = 0°$ and $\alpha' = 45°$. In analyzing the results with QWP compensation (Fig. 9b) and taking the idler's polarization angles to be $\beta = 154.5°$ and $\beta' = 109.5°$, we obtain $S = 2.711 \pm 0.021$. For the analysis of the polarization fringes without QWP compensation (Fig. 9a), we take $\alpha = 0°$, $\alpha' = 45°$, $|\beta - \beta'| = 45°$ and allow β to vary. We find the best case is $S = 1.600 \pm 0.033$, which does not exceed the non-classical bound $S \geq 2$. In general, the relative angles $|\alpha - \alpha'|$ and $|\beta - \beta'|$ should be equal to each other but not necessarily equal to 45° [49]. Using numerical modeling of the theoretical fringes with $\epsilon = 0.455$ and $\phi = 0.45\pi$ (Fig. 9c), best-case-value $S = 2.024$ is found for $|\alpha - \alpha| = |\beta - \beta'| = -17°$, which implies that the non-QWP compensated state does violate Bell's inequality, but only weakly. After numerically applying the QWP compensation and taking the relative polarization angles for the signal and idler to be 45°, $S = 2.817$, a significant increase. Using the QWP compensation, the S parameter can be significantly improved, leading to higher quality polarization entanglement.

Acknowledgment. We thank Thomas Gerrits and Cory Nunn for helpful discussions.

Disclosures. The authors declare no conflicts of interest. Certain commercial equipment or materials may be identified in this paper in order to specify device fabrication, the experimental procedure, and data analysis adequately. Such identification is not intended to imply endorsement by the National Institute of Standards and Technology; neither is it intended to imply that the equipment nor the material identified are necessarily the best available.

Data availability. Data underlying the results presented in this paper are not publicly available at this time but may be obtained from the authors upon reasonable request.

References

1. H. J. Kimble, "The quantum internet," Nature **453**, 1023 – 1030 (2008).
2. I. Marcikic, H. de Riedmatten, W. Tittel, *et al.*, "Distribution of time-bin entangled qubits over 50 km of optical fiber," Phys. Rev. Lett. **93**, 180502 (2004).
3. S. Wengerowsky, S. K. Joshi, F. Steinlechner, *et al.*, "An entanglement-based wavelength-multiplexed quantum communication network," Nature **564**, 225–228 (2018).
4. D. Gottesman, T. Jennewein, and S. Croke, "Longer-baseline telescopes using quantum repeaters," Phys. Rev. Lett. **109**, 070503 (2012).
5. S. Bartolucci, P. Birchall, H. Bombín, *et al.*, "Fusion-based quantum computation," Nat. Commun. **14**, 912 (2023).
6. P. G. Kwiat, K. Mattle, H. Weinfurter, *et al.*, "New high-intensity source of polarization-entangled photon pairs," Phys. Rev. Lett. **75**, 4337–4341 (1995).
7. P. G. Kwiat, E. Waks, A. G. White, *et al.*, "Ultrabright source of polarization-entangled photons," Phys. Rev. A **60**, R773–R776 (1999).
8. T. Kim, M. Fiorentino, and F. N. C. Wong, "Phase-stable source of polarization-entangled photons using a polarization sagnac interferometer," Phys. Rev. A **73**, 012316 (2006).
9. M. Fiorentino and R. G. Beausoleil, "Compact sources of polarization-entangled photons," Opt. Express **16**, 20149–20156 (2008).
10. P. G. Evans, R. S. Bennink, W. P. Grice, *et al.*, "Bright source of spectrally uncorrelated polarization-entangled photons with nearly single-mode emission," Phys. Rev. Lett. **105**, 253601 (2010).
11. T. Suhara, G. Nakaya, J. Kawashima, and M. Fujimura, "Quasi-phase-matched waveguide devices for generation of postselection-free polarization-entangled twin photons," IEEE Photonics Technol. Lett. **21**, 1096–1098 (2009).

12. F. Steinlechner, P. Trojek, M. Jofre, *et al.*, "A high-brightness source of polarization-entangled photons optimized for applications in free space," Opt. Express **20**, 9640–9649 (2012).
13. J. E. Sharping, K. F. Lee, M. A. Foster, *et al.*, "Generation of correlated photons in nanoscale silicon waveguides," Opt. Express **14**, 12388–12393 (2006).
14. J. W. Silverstone, R. Santagati, D. Bonneau, *et al.*, "Qubit entanglement between ring-resonator photon-pair sources on a silicon chip," Nat. Commun. **6**, 7948 (2015).
15. Y. Shih, "Entangled photons," IEEE J. Sel. Top. Quantum Electron. **9**, 1455–1467 (2003).
16. P. Trojek and H. Weinfurter, "Collinear source of polarization-entangled photon pairs at nondegenerate wavelengths," Appl. Phys. Lett. **92**, 211103 (2008).
17. W. P. Grice, A. B. U'Ren, and I. A. Walmsley, "Eliminating frequency and space-time correlations in multiphoton states," Phys. Rev. A **64**, 063815 (2001).
18. E. Meyer-Scott, N. Montaut, J. Tiedau, *et al.*, "Limits on the heralding efficiencies and spectral purities of spectrally filtered single photons from photon-pair sources," Phys. Rev. A **95**, 061803 (2017).
19. A. Anwar, C. Perumangatt, F. Steinlechner, *et al.*, "Entangled photon-pair sources based on three-wave mixing in bulk crystals," Rev. Sci. Instruments **92**, 041101 (2021).
20. W. Ueno, F. Kaneda, H. Suzuki, *et al.*, "Entangled photon generation in two-period quasi-phase-matched parametric down-conversion," Opt. Express **20**, 5508–5517 (2012).
21. F. Kaneda, H. Suzuki, R. Shimizu, and K. Edamatsu, "Direct generation of frequency-bin entangled photons via two-period quasi-phase-matched parametric downconversion," Opt. Express **27**, 1416–1424 (2019).
22. F. Laudenbach, S. Kalista, M. Hentschel, *et al.*, "A novel single-crystal & single-pass source for polarisation- and colour-entangled photon pairs," Sci. Reports **7**, 7235 (2017).
23. P. Hendra, J. R. León-Torres, V. F. Gili, and M. Gräfe, "Rubidium-doped $\mathrm{KTiOPO_4}$ waveguides as a dual-type photon-pair source," J. Opt. Soc. Am. B **42**, 1976–1981 (2025).
24. Y.-X. Gong, Z.-D. Xie, P. Xu, *et al.*, "Compact source of narrow-band counterpropagating polarization-entangled photon pairs using a single dual-periodically-poled crystal," Phys. Rev. A **84**, 053825 (2011).
25. K. Thyagarajan, J. Lugani, S. Ghosh, *et al.*, "Generation of polarization-entangled photons using type-II doubly periodically poled lithium niobate waveguides," Phys. Rev. A **80**, 052321 (2009).
26. J. Shi, S.-J. Yun, Y.-F. Bai, *et al.*, "Compact generation of polarization-frequency hyperentangled photon pairs by using quasi-phase-matched lithium niobate," Opt. Commun. **285**, 5549–5553 (2012).
27. P. S. Kuo, T. Gerrits, V. B. Verma, and S. W. Nam, "Spectral correlation and interference in non-degenerate photon pairs at telecom wavelengths," Opt. Lett. **41**, 5074–5077 (2016).
28. P. S. Kuo, V. B. Verma, and S. W. Nam, "Demonstration of a polarization-entangled photon-pair source based on phase-modulated PPLN," OSA Continuum **3**, 295–304 (2020).
29. C.-W. Sun, S.-H. Wu, J.-C. Duan, *et al.*, "Compact polarization-entangled photon-pair source based on a dual-periodically-poled Ti:$\mathrm{LiNbO_3}$ waveguide," Opt. Lett. **44**, 5598–5601 (2019).
30. P. S. Kuo, C. S. S. P. Kumar, D. V. Reddy, *et al.*, "Domain-engineered, aperiodically-poled KTP for polarization-entangled photons," in *CLEO 2025,* (Optica Publishing Group, 2025), p. FF107_5.
31. A. Shukhin, I. Hurvitz, L. Vidro, *et al.*, "Direct polarization-entangled photon pair generation using domain-engineered nonlinear crystals," Opt. Quantum **3**, 487–494 (2025).
32. R. Shiloh and A. Arie, "Spectral and temporal holograms with nonlinear optics," Opt. Lett. **37**, 3591–3593 (2012).
33. A. Leshem, R. Shiloh, and A. Arie, "Experimental realization of spectral shaping using nonlinear optical holograms," Opt. Lett. **39**, 5370–5373 (2014).
34. M. Fejer, G. Magel, D. Jundt, and R. Byer, "Quasi-phase-matched second harmonic generation: tuning and tolerances," IEEE J. Quantum Electron. **28**, 2631–2654 (1992).
35. M. H. Chou, K. R. Parameswaran, M. M. Fejer, and I. Brener, "Multiple-channel wavelength conversion by use of engineered quasi-phase-matching structures in $\mathrm{LiNbO_3}$ waveguides," Opt. Lett. **24**, 1157–1159 (1999).
36. M. Asobe, O. Tadanaga, H. Miyazawa, *et al.*, "Multiple quasi-phase-matched $\mathrm{LiNbO_3}$ wavelength converter with a continuously phase-modulated domain structure," Opt. Lett. **28**, 558–560 (2003).
37. K. Fradkin, A. Arie, A. Skliar, and G. Rosenman, "Tunable midinfrared source by difference frequency generation in bulk periodically poled $\mathrm{KTiOPO_4}$," Appl. Phys. Lett. **74**, 914–916 (1999).
38. F. König and F. N. C. Wong, "Extended phase matching of second-harmonic generation in periodically poled $\mathrm{KTiOPO_4}$ with zero group-velocity mismatch," Appl. Phys. Lett. **84**, 1644–1646 (2004).
39. S. Emanueli and A. Arie, "Temperature-dependent dispersion equations for $\mathrm{KTiOPO_4}$ and $\mathrm{KTiOAsO_4}$," Appl. Opt. **42**, 6661–6665 (2003).
40. S. V. Polyakov and A. L. Migdall, "High accuracy verification of a correlated-photon-based method for determining photon-counting detection efficiency," Opt. Express **15**, 1390–1407 (2007).
41. W. B. Whitten and H. H. Ross, "Fiber optic waveguides for time-of-flight optical spectrometry," Anal. Chem. **51**, 417–419 (1979).
42. M. Avenhaus, A. Eckstein, P. J. Mosley, and C. Silberhorn, "Fiber-assisted single-photon spectrograph," Opt. Lett. **34**, 2873–2875 (2009).
43. A. Aspect, P. Grangier, and G. Roger, "Experimental realization of Einstein-Podolsky-Rosen-Bohm gedankenexperiment: A new violation of Bell's inequalities," Phys. Rev. Lett. **49**, 91–94 (1982).
44. J. F. Clauser, M. A. Horne, A. Shimony, and R. A. Holt, "Proposed experiment to test local hidden-variable theories,"

Phys. Rev. Lett. **23**, 880–884 (1969).
45. M. Le Bellac, *A Short Introduction to Quantum Information and Quantum Computation* (Cambridge University Press, Cambridge, 2006).
46. J. Peatross and M. Ware, *Physics of Light and Optics* (optics.byu.edu, 2015).
47. J. B. Altepeter, E. R. Jeffrey, and P. G. Kwiat, “Photonic state tomography,” (Academic Press, 2005), pp. 105–159.
48. P. S. Kuo, “Effect of amplitude mismatch on entanglement visibility in photon-pair sources,” in *OSA Advanced Photonics Congress (AP) 2020 (IPR, NP, NOMA, Networks, PVLED, PSC, SPPCom, SOF),* (Optica Publishing Group, 2020), p. ITu4A.15.
49. P. H. Eberhard, “Background level and counter efficiencies required for a loophole-free Einstein-Podolsky-Rosen experiment,” Phys. Rev. A **47**, R747–R750 (1993).